

The surface layer of Sr_2RuO_4 : A two-dimensional model system for magnetic-field-tuned quantum criticality

Carolina A. Marques^{1, †}, Luke C. Rhodes^{1, †}, Rosalba Fittipaldi², Veronica Granata³,

Chi Ming Yim¹, Renato Buzio⁴, Andrea Gerbi⁴, Antonio Vecchione², Andreas W. Rost^{1, 5},

Peter Wahl^{1, *}

¹ SUPA, School of Physics and Astronomy, University of St Andrews, North Haugh, St Andrews, KY16 9SS, United Kingdom.

² CNR-SPIN, UOS Salerno, Via Giovanni Paolo II 132, Fisciano, I-84084, Italy.

³ Dipartimento di Fisica “E. R. Caianiello”, Università di Salerno, I-84084 Fisciano, Salerno, Italy.

⁴ CNR-SPIN, Corso F.M. Perrone 24, Genova, 16152, Italy.

⁵ Max-Planck-Institute for Solid State Research, Heisenbergstr. 1, 70569 Stuttgart, Germany

* Correspondence to: wahl@st-andrews.ac.uk.

† These authors contributed equally.

Many of the exciting properties of strongly correlated materials are intricately linked to quantum critical points in their phase diagram. This includes phenomena such as high temperature superconductivity,^{1,2} unconventional superconductivity in heavy fermion materials,³ as well as exotic nematic states in $\text{Sr}_3\text{Ru}_2\text{O}_7$.⁴ One of the experimentally most successful pathways to reaching a quantum critical point is tuning by magnetic field allowing studies under well-controlled conditions on ultra-clean samples. Yet, spectroscopic evidence of how the electronic states change across a field-tuned quantum phase transition, and what the importance of quantum fluctuations is, is not available so far. Here we show that the surface layer of Sr_2RuO_4 is an ideal two-dimensional model

system for a field-tuned quantum phase transition. We establish the existence of four van Hove singularities in close proximity to the Fermi energy, linked intricately to checkerboard charge order and nematicity of the electronic states. Through magnetic field, we can tune the energy of one of the van Hove singularities, with the Lifshitz transition extrapolated at ~ 32 T. Our experiments open up the ability to directly study spectroscopically the role of quantum fluctuations at a field-tuned quantum phase transition in an effectively 2D strongly correlated electron material. Our results further have implications for what the leading instability in Sr_2RuO_4 is, and hence for understanding the enigmatic superconductivity in this material.

The occurrence of quantum criticality is often connected to van Hove singularities (vHs) in the electronic structure close to the Fermi energy (E_F). Tuning such a van Hove singularity to the Fermi energy leads to a Lifshitz transition that can explain many of the exotic properties of quantum materials⁵⁻⁹. The Lifshitz transition is associated with a large change in the density of states (DOS) at the Fermi level together with a change in Fermi surface topology, leading to a quantum phase transition. For a magnetic-field tuned Lifshitz transition, this mechanism requires a van-Hove singularity within a few meV of E_F , so that a Zeeman splitting can drive one spin sub-band of the vHs to E_F as illustrated in Figure 1a. Yet in many materials, it remains unclear whether the properties attributed to the quantum critical point are driven by quantum fluctuations, or simply a consequence of the Lifshitz transition in a single particle picture. Spectroscopic detection of the changes in the DOS in such a scenario would enable clarification of the role of quantum fluctuations in the Lifshitz transition, as well as provide the opportunity to test theories aiming at describing quantum criticality and the role of quantum fluctuations.

In this work, we show that the surface layer of Sr_2RuO_4 is an ideal model system to study a magnetic-field tuned Lifshitz transition. Whilst the bulk of Sr_2RuO_4 is a superconductor with a transition temperature $T_c \sim 1.5$ K,¹⁰ the clean surface exhibits a reconstruction suppressing superconductivity.¹¹ We use ultra-low temperature scanning tunneling microscopy (STM) to demonstrate that the electronic structure of the surface layer enters a new emergent phase that cannot be explained simply by the structural change of the surface. We identify a checkerboard charge order concomitant with nematicity of the low energy electronic structure, giving rise to four vHs within 5 mV of the Fermi energy. In tunneling spectra in magnetic fields up to 13.4 T and at temperatures down to 50 mK, we observe a clear magnetic-field-induced splitting of the most prominent vHs, which can be tuned towards the Fermi level.

Results

The crystal structure of Sr_2RuO_4 consists of single layers of RuO_2 sandwiched between SrO layers, with a tetragonal unit cell.¹² The bulk Fermi surface of Sr_2RuO_4 , represented in Figure 1b, has been established by quantum oscillations¹³ and confirmed by angle-resolved photoemission spectroscopy (ARPES)^{14,15}. It is mainly made up of the $4d$ t_{2g} states of the Ru atoms, where the 2D d_{xy} band (yellow line) has a vHs at the M-point of the Brillouin zone (BZ). The energy of the bulk vHs has been estimated at about 14 meV above E_F ¹⁶ and leads to a peak in the DOS (solid line in Figure 1c).

The surface layer of Sr_2RuO_4 exhibits a 6° rotation of the RuO_6 octahedra¹⁷ (Figure 1c, left inset). This rotation doubles the size of the unit cell and modifies the Fermi surface (Figure 1d) and band dispersion so that the vHs is shifted below E_F ¹⁴ (Figure 1c, dashed line).

Figure 1e shows a topographic image of Sr_2RuO_4 , recorded at a temperature of 76mK, showing a SrO-terminated surface^{18,19} with atomic resolution and demonstrating a low concentration of point defects (less than 0.1%). We find defects at the Ru site with two distinct orientations due to the octahedral rotation. The Fourier transform of the topography (upper inset in Figure 1e), shows the presence of quasiparticle interference (QPI), as well as Bragg peaks at $(0, 2\pi)$ due to the Sr lattice, and peaks at (π, π) from a modulation of the charge

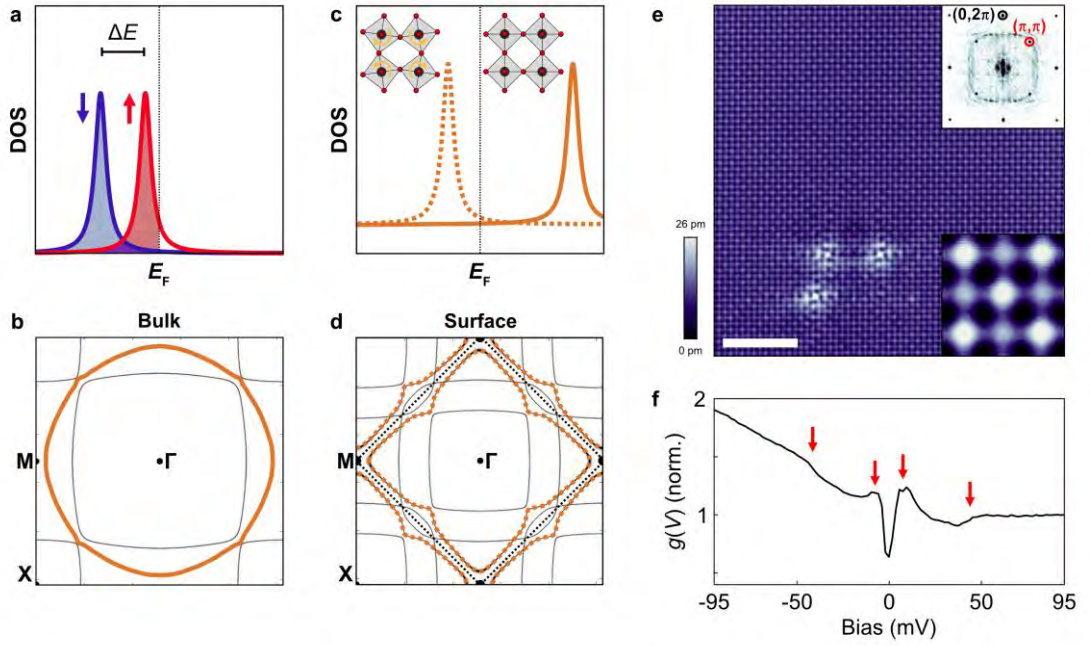


Figure 1: Field tuning of a van Hove singularity and the surface of Sr_2RuO_4 . *a*, Representation of the splitting of a van Hove singularity in magnetic field \mathbf{B} . Red and blue curves represent the vHs with opposing spin species split by $\Delta E = g^* \mu_B B_z$. *b*, Calculated bulk Fermi surface of Sr_2RuO_4 with the d_{xy} band highlighted in yellow and the d_{xz}/d_{yz} bands shown in black. *c*, Representation of the signature in DOS of the vHs of bulk Sr_2RuO_4 (solid line), which occurs above E_F . Insets show the RuO_6 octahedra, which in the bulk (right side) have the same orientation at each lattice site (black=Ru, red=O). The rotation of the RuO_6 octahedra at the surface, shown on the left, shifts the vHs below E_F (dashed line). *d*, Calculated Fermi surface of the surface layer of Sr_2RuO_4 , showing the folded d_{xy} band in yellow. The dashed black lines represent the new Brillouin zone due to the surface reconstruction. *e*, Topography of the surface of Sr_2RuO_4 , showing the Sr square lattice superimposed with an intensity modulation between adjacent Sr atoms, shown in more detail in the lower inset ($V_{\text{set}} = -5$ mV, $I_{\text{set}} = 50$ pA, scale bar: 5 nm). The upper inset shows the corresponding Fourier transform with Bragg peaks corresponding to the Sr lattice at $(0, 2\pi)$ (black circle). Additional peaks at (π, π) (red circle) coincide with the periodicity of the reconstructed surface (reciprocal lattice vectors in units of $1/a$, where a is the lattice parameter of Sr_2RuO_4). *f*, Tunneling spectrum $g(V)$ acquired on the SrO-terminated surface of Sr_2RuO_4 , measured at 76 mK. Red arrows mark the characteristic spectroscopic features of this termination ($V_{\text{set}} = 100$ mV, $I_{\text{set}} = 265.2$ pA, $V_L = 1.75$ mV).

density (lower inset in Figure 1e) with the periodicity of the surface reconstruction. This modulation has been observed previously at the surface of Sr_2RuO_4 ,¹⁸ as well as at that of $\text{Sr}_3\text{Ru}_2\text{O}_7$.²⁰ However, there is no obvious explanation for how the octahedral rotation leads to a charge modulation.

A typical differential conductance spectrum $g(V)$ in the range ± 80 mV is presented in Figure 1f. Here, kink- and gap-like features are observed at ± 43 meV and ± 5 meV respectively. The latter is associated with a reduction of the differential conductance by almost 30%. The spectra, as well as the absence of a superconducting gap, are in agreement with previous reports^{21–23}.

The additional modulation of the charge density leads to pronounced signatures in spectroscopic maps: while topographic images obtained at positive bias voltage show predominantly the Sr lattice (Figure 2a), differential conductance maps exhibit a clear checkerboard charge modulation superimposed to this lattice at bias voltages close to E_F (Figure 2b, c). The checkerboard exhibits a contrast inversion across the Fermi energy. We plot in Figure 2d the energy dependence of the intensity of the checkerboard analyzed through a phase-referenced Fourier transformation (PR FFT, see S2C), which provides information about the amplitude and phase of the modulation. The amplitude of the checkerboard exhibits a pronounced maximum at -3.5 mV with a width of only about 1 mV and a weaker maximum at $+3.5$ mV of similar width but with opposite phase. The phase change is consistent with what one would expect for a charge density wave.²⁴

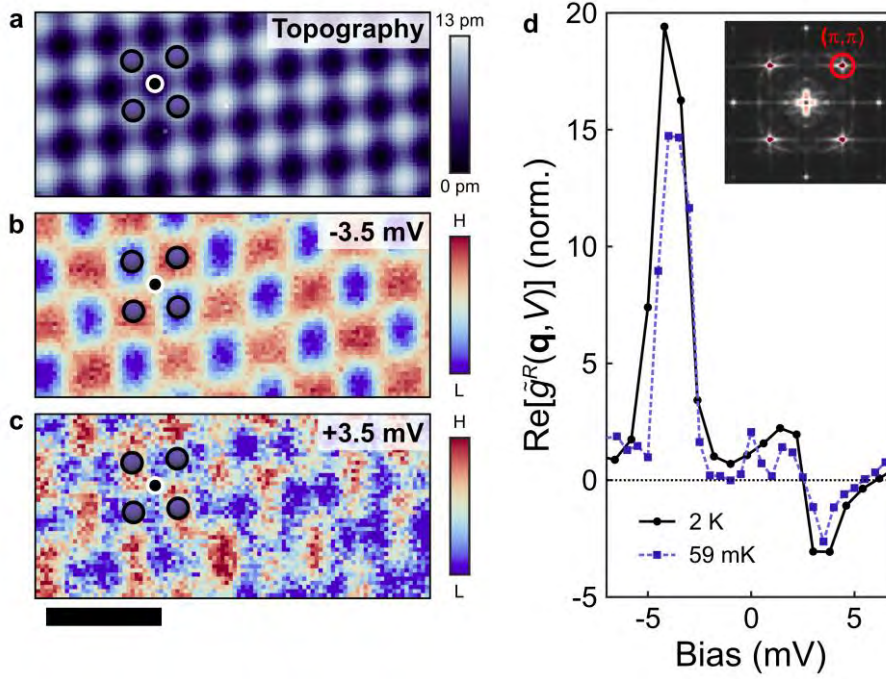


Figure 2: Checkerboard charge order in the surface layer of Sr_2RuO_4 . *a*, Topography obtained at $V_s=7$ mV showing the Sr square lattice. *b*, *c*, Real-space spectroscopic maps $g(\mathbf{r}, V)$ in the same region as in *a* at $V=-3.5$ mV and $V=+3.5$ mV, respectively. At -3.5 mV, a strong checkerboard charge order is observed. At +3.5 mV, the order is seen with opposite phase ($T=56$ mK, $V_{\text{set}}=7.0$ mV, $I_{\text{set}}=250$ pA, $V_L=495$ μ V, scale bar: 1 nm). *d*, Energy dependence of the Fourier peak at $\mathbf{q}_{\text{ckb}}=(\pi, \pi)$ due to the checkerboard charge order in the phase-referenced Fourier transformation. \mathbf{q}_{ckb} is indicated by a red circle in the inset showing the Fourier transformation $\tilde{g}(\mathbf{q}, V)$ of the conductance map. Two peaks at -3.5 mV and +3.5 mV with opposite phase and a full width at half maximum of ~ 1 mV can be seen for maps taken at $T=2$ K and 56 mK. The intensity of the two maps is normalized to the value at the bias setpoint (see S2 for details).

Comparison of the checkerboard charge order centred at the Sr sites with the structure of the surface layer shows that the emergence of this charge order is equivalent to a reduction of C_4 symmetry to C_2 symmetry (Figure 3a) as a consequence of the octahedral rotation. The broken C_4 symmetry means that the oxygen atoms become inequivalent in the $[10]$ and $[01]$ directions, as indicated in Figure 3a, resulting in nematicity of the low energy electronic states. This emergent nematicity is confirmed experimentally through unidirectional periodic modulations with atomic periodicity (Figure 3b, c) and anisotropy of the low- q quasi-particle interference (Figure 3d-i). The atomic scale symmetry breaking reveals that for changes in the

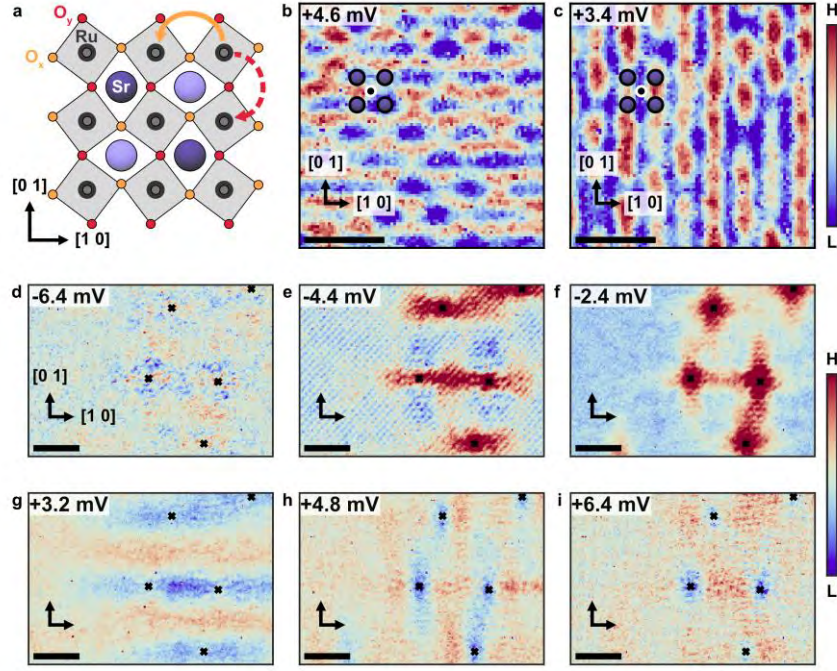


Figure 3: Nematicity and the equivalence of C_4 symmetry breaking. *a*, Model of the surface atomic structure with the checkerboard charge order. The charge order on the Sr lattice combined with the octahedral rotations leads to a broken C_4 symmetry, which renders the oxygen atoms along the $[10]$ and $[01]$ directions (labelled O_x and O_y) inequivalent. *b*, *c*, Nematicity in the atomic scale charge modulations ($T=1.8$ K, $V_{set}=7.8$ mV, $I_{set}=500$ pA, $V_L=370$ μ V, scale bar: 1nm). *d-i* Real space images showing directional quasi-particle interference near defects ($T=56$ mK, $V_{set}=6.4$ mV, $I_{set}=225$ pA, $V_L=398$ μ V, scale bar: 5nm).

bias voltage of about 1mV the atomic-scale unidirectional periodicity changes direction between the high-symmetry directions $[10]$ and $[01]$. This is also confirmed in the intensity of the atomic peaks (Fig. S4). The symmetry breaking of long-wavelength quasi-particle interference is seen in a real-space map around four defects (Figure 3d-i, defects marked by black crosses) and reveals a change from predominant quasiparticle scattering along $[10]$ to scattering along $[01]$ and back as a function of energy.

To understand the microscopic consequences nematicity and the observed charge modulation have on the electronic structure of this system, we have performed tight-binding simulations of the band structure of the surface of Sr_2RuO_4 , accounting for the surface

reconstruction and with hopping parameters optimized against ARPES data¹⁵. The surface reconstruction and the checkerboard charge order (Figure 2) are accounted for by including a weak intraband hybridization (Δ_{hyb}). We account for the broken symmetry along the [10] and [01] lattice directions (Figure 3) through inclusion of a phenomenological nematic order parameter $\Delta_{\text{nem}} = \delta_{\text{nem}}(\cos(k_x) - \cos(k_y))$, which we apply only to the relevant d_{xy} orbital. A similar order parameter has previously been introduced to describe nematicity in $\text{Sr}_3\text{Ru}_2\text{O}_7$.²⁵ The full Hamiltonian is then

$$H(k) = \begin{pmatrix} H_{\text{Ru}}(\mathbf{k}) + \Delta_{\text{nem}}\hat{I}_{xy} & \Delta_{\text{hyb}}\hat{I} \\ \Delta_{\text{hyb}}\hat{I} & H_{\text{Ru}}(\mathbf{k} + \mathbf{Q}) + \Delta_{\text{nem}}\hat{I}_{xy} \end{pmatrix}, \quad (1)$$

where $H_{\text{Ru}}(\mathbf{k})$ is the Hamiltonian for the ruthenium $4d$ bands in the unreconstructed Brillouin zone²⁶, and $\mathbf{Q} = (\pi, \pi)$ accounts for the doubling of the unit cell (for details see S3). The band structure, calculated from Eq. 1, is presented for the most relevant part of the Brillouin zone around the M point in Figure 4a. We follow the notation by van Hove²⁷ to label the resulting four van Hove singularities in the band structure: nematicity results in two saddle points, $\mathcal{S}1$ and $\mathcal{S}2$, on the high symmetry axis at the M point, whereas hybridization leads to a partial gap structure with a band maximum \mathcal{M} and an additional saddle point $\mathcal{S}3$ around E_F . This can be seen from a 3D representation of the band structure around the M point (Figure 4b). The partial drop in the $g(V)$ spectrum around E_F , observed in Figure 1f, is naturally explained by the hybridization of the Ru d_{xy} -bands caused by the doubling of the unit cell. These four singularities lead to maxima in the density of states (see Figure 4c) in excellent agreement with the structure of the low energy $g(V)$ spectrum.

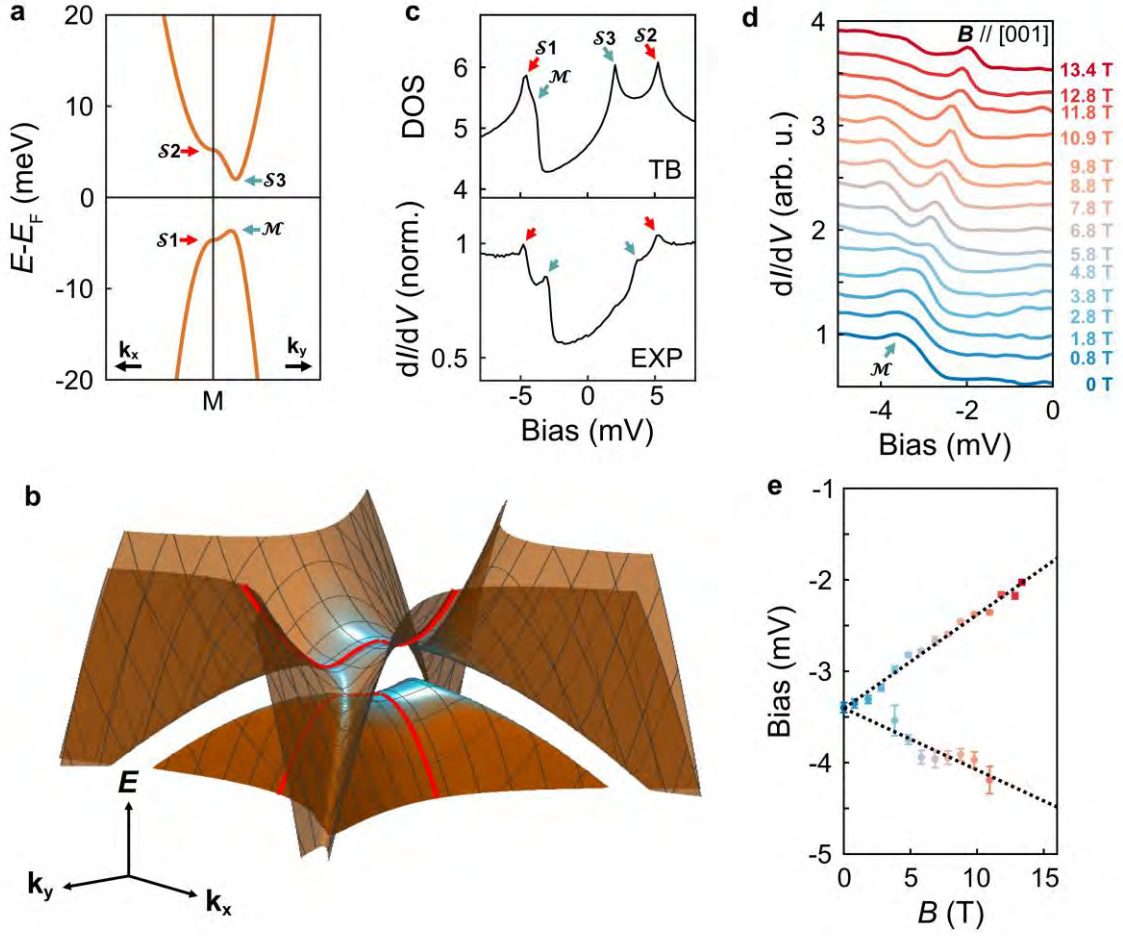


Figure 4: Identification and field-tuning of van-Hove singularities. *a, b*, Band structure around the M point from the tight-binding model of the surface of Sr_2RuO_4 including an intraband hybridization potential and nematic order parameter as discussed in the main text. *b* shows the three dimensional band dispersion around the M point within 20 meV of E_F . The blue shaded regions indicate the location of the vHs, and reveal the presence of three saddle-point-type vHs's and one maxima-type-vHs (labelled S1, S2, S3 and \mathcal{M} in *a*). Red lines indicate the path shown in *a*. *c*, Upper panel: Density of states calculated from the model in *a* and *b*, highlighting the four vHs. The lower panel shows a tunneling spectrum ($V_{\text{set}}=8.2$ mV, $I_{\text{set}}=500.2$ pA, $V_L=155$ μV , $T=56$ mK), revealing a gap-like structure and four distinct peaks which can be associated with the predicted vHs. *d*, Tunneling spectra recorded at a temperature of 76mK in magnetic fields normal to the surface (parallel to the c-axis of the crystal) from 0T to 13.4T, focusing on the most intense vHs (\mathcal{M}) at -3.4mV ($V_{\text{set}}=5$ mV, $I_{\text{set}}=225$ pA, $V_L=100$ μV). *e*, Peak position of \mathcal{M} as a function of field extracted from fits of Lorentzian peaks to the spectra (see supplementary S4). It reveals a splitting and linear magnetic field dependence as expected for a Zeeman-split state with $g^*\sim 3$ (error bars are 95% confidence intervals of the fits).

Having identified the presence and origin of the van Hove singularities at the surface of Sr_2RuO_4 , we investigate the influence of an applied magnetic field, focusing on the behavior

of the most prominent vHs, \mathcal{M} , at -3.4 mV. Figure 4d shows tunneling spectra recorded in magnetic fields from 0T to 13.4T, applied perpendicular to the surface. The spectra reveal a clear splitting of the vHs with increasing magnetic field. In Figure 4e, the field-dependence of the energy of the vHs reveals a linear behavior as expected for a Zeeman-like splitting. We find the slope to be +0.10 mV/T for the peak moving towards the Fermi energy and -0.07mV/T for the one moving away. The difference in slope can be attributed to an overall chemical potential shift of the d_{xy} band of $17\mu\text{V/T}$ to ensure charge conservation. Taking this into account, we find a g -factor of $g^* \sim 3$ (with the splitting $\Delta E = g^* \mu_B B_z$). This value is consistent with the known Wilson ratio of bulk Sr_2RuO_4 .²⁸ From our experimental data, we can extrapolate that the vHs will cross the Fermi energy at a magnetic field of about 32T. At this field, the surface layer is expected to undergo a Lifshitz transition. As the energy of the van Hove singularity is associated with the checkerboard charge order, once it is split in a magnetic field, the charge order becomes spin-polarized. Our measurements demonstrate that the electronic structure of the reconstructed surface layer of Sr_2RuO_4 has all the ingredients for quantum critical behavior as described in the model in Figure 1a: (1) a vHs close to the Fermi energy, (2) the energy of the vHs can be tuned by magnetic field towards the Fermi energy, and (3) a Lifshitz transition of the electronic structure within reach of available magnetic fields.

Discussion

Our measurements show how the electronic structure of a two-dimensional model system evolves on approaching a magnetic-field induced Lifshitz transition, making it effectively a quantum simulator to study field-tuned quantum phase transitions. We can explain the surface electronic structure well by a phenomenological tight-binding model that incorporates the two orders we detect, nematicity and checkerboard charge order and reproduces all features we observe in our data. It naturally explains the pronounced gap-like

feature seen in tunneling spectra. What the model does not provide is an explanation for the origin of the checkerboard order and nematicity, and which of the two dominates, if either. Possible mechanisms include (1) nematicity driven by electron correlations, (2) charge order driven by nesting or a lattice distortion, (3) a cooperative effect of both, and (4) an antiferromagnetic order with formation of a spin-density wave, which stabilizes the checkerboard order and nematicity. For the first three scenarios, one would expect a significant structural distortion accompanying these, as is seen for charge density waves or nematicity in other systems. A structural distortion in the surface layer of Sr_2RuO_4 beyond the octahedral rotation has not been reported so far.²⁹ In a scenario where magnetic order or fluctuations drive nematicity and charge order, one would still expect a structural distortion, though much smaller.

A comparison with $\text{Sr}_3\text{Ru}_2\text{O}_7$ reveals intriguing parallels: $\text{Sr}_3\text{Ru}_2\text{O}_7$ exhibits a similar (albeit larger) octahedral rotation, and the energy of the vHs as detected by ARPES occurs at an energy below E_F ³⁰, close to the energy at which we find the dominant vHs in the surface layer of Sr_2RuO_4 . Due to stronger correlations and a g -factor of $g^* \approx 14.6$ in $\text{Sr}_3\text{Ru}_2\text{O}_7$,³¹ the vHs can be tuned to the Fermi energy at 8T, whereas in the surface layer of Sr_2RuO_4 , we find a g -factor that is almost 4 times smaller. Consequently, the vHs is expected to reach the Fermi energy only at 32T. It remains to be seen whether the parallels go any further when the surface layer in Sr_2RuO_4 undergoes the Lifshitz transition. There are also important differences though, including that the system we report here is strictly two-dimensional which puts the criticality of the Lifshitz transition into a different universality class than what is expected for the bulk of $\text{Sr}_3\text{Ru}_2\text{O}_7$.

Consistent with previous studies of the reconstructed surface,^{21,22} we do not observe any evidence for superconductivity, indicating that the emergent electronic order suppresses superconductivity in the surface layer. This may imply that the density of states of the d_{xy} band around E_F , which becomes gapped out at the surface, and the fluctuations associated with the reconstruction play a crucial factor in superconducting pairing. This scenario naturally results in a competition of nematicity and the charge density modulations with superconductivity, reminiscent to what is found in other strongly correlated electron systems^{3,32,33}. Understanding the leading superconducting instability in this highly debated material therefore undoubtedly will have to account for this susceptibility towards density wave formation as observed in other unconventional superconductors.

Conclusion

Using the surface layer of Sr_2RuO_4 as a two-dimensional model system to study magnetic-field induced critical points and Lifshitz transitions provides a new well-controlled test bed to compare microscopic theories to experiment. Because the emergent surface phase is strictly two-dimensional, limited to the surface layer, all relevant information about the electronic states across the quantum phase transition are accessible spectroscopically. Magnetic-field tuned Lifshitz transitions have been proposed to be at the heart of the quantum critical behavior in a range of heavy fermion and strongly correlated electron materials, yet the ability to spectroscopically trace the electronic structure across a field-tuned quantum phase transition has remained elusive. Given the sensitivity of the energy of the van-Hove singularity in Sr_2RuO_4 to uniaxial strain,³⁴ we expect that the magnetic field at which the surface undergoes the quantum phase transition can be reduced substantially by combining uniaxial strain with magnetic field. This creates the opportunity to spectroscopically verify the role of quantum fluctuations near a field-tuned quantum critical point, and provides important insights into the

leading instabilities of Sr_2RuO_4 with important implications for its enigmatic superconducting state.

1. Michon, B. *et al.* Thermodynamic signatures of quantum criticality in cuprate superconductors. *Nature* **567**, 218–222 (2019).
2. Cooper, R. A. *et al.* Anomalous Criticality in the Electrical Resistivity of $\text{La}_{2-x}\text{Sr}_x\text{CuO}_4$. *Science* **323**, 603–607 (2009).
3. Mathur, N. D. *et al.* Magnetically mediated superconductivity in heavy fermion compounds. *Nature* **394**, 39–43 (1998).
4. Borzi, R. A. *et al.* Formation of a Nematic Fluid at High Fields in $\text{Sr}_3\text{Ru}_2\text{O}_7$. *Science* **315**, 214–217 (2007).
5. Lifshitz, I. M. Anomalies of electron characteristics of a metal in the high pressure region. *J. Exp. Theor. Phys.* **11**, 1130–1135 (1960).
6. Yamaji, Y., Misawa, T. & Imada, M. Quantum and Topological Criticalities of Lifshitz Transition in Two-Dimensional Correlated Electron Systems. *J. Phys. Soc. Jpn.* **75**, 094719 (2006).
7. Viola Kusminskiy, S., Beach, K. S. D., Castro Neto, A. H. & Campbell, D. K. Mean-field study of the heavy-fermion metamagnetic transition. *Phys. Rev. B* **77**, 094419 (2008).
8. Hackl, A. & Vojta, M. Zeeman-Driven Lifshitz Transition: A Model for the Experimentally Observed Fermi-Surface Reconstruction in YbRh_2Si_2 . *Phys. Rev. Lett.* **106**, 137002 (2011).

9. Efremov, D. V. *et al.* Multicritical Fermi Surface Topological Transitions. *Phys. Rev. Lett.* **123**, 207202 (2019).
10. Maeno, Y. *et al.* Superconductivity in a layered perovskite without copper. *Nature* **372**, 532–534 (1994).
11. Firmo, I. A. *et al.* Evidence from tunneling spectroscopy for a quasi-one-dimensional origin of superconductivity in Sr_2RuO_4 . *Phys. Rev. B* **88**, 134521 (2013).
12. Lichtenberg, F., Catana, A., Mannhart, J. & Schlom, D. G. Sr_2RuO_4 : A metallic substrate for the epitaxial growth of $\text{YBa}_2\text{Cu}_3\text{O}_{7-\delta}$. *Appl. Phys. Lett.* **60**, 1138–1140 (1992).
13. Mackenzie, A. P. *et al.* Quantum Oscillations in the Layered Perovskite Superconductor Sr_2RuO_4 . *Phys. Rev. Lett.* **76**, 3786–3789 (1996).
14. Veenstra, C. N. *et al.* Determining the Surface-To-Bulk Progression in the Normal-State Electronic Structure of Sr_2RuO_4 by Angle-Resolved Photoemission and Density Functional Theory. *Phys. Rev. Lett.* **110**, 097004 (2013).
15. Tamai, A. *et al.* High-Resolution Photoemission on Sr_2RuO_4 Reveals Correlation-Enhanced Effective Spin-Orbit Coupling and Dominantly Local Self-Energies. *Phys. Rev. X* **9**, 021048 (2019).
16. Shen, K. M. *et al.* Evolution of the Fermi Surface and Quasiparticle Renormalization through a van Hove Singularity in $\text{Sr}_{2-y}\text{La}_y\text{RuO}_4$. *Phys. Rev. Lett.* **99**, 187001 (2007).
17. Matzdorf, R. *et al.* Ferromagnetism Stabilized by Lattice Distortion at the Surface of the p -Wave Superconductor Sr_2RuO_4 . *Science* **289**, 746–748 (2000).

18. Pennec, Y. *et al.* Cleaving-Temperature Dependence of Layered-Oxide Surfaces. *Phys. Rev. Lett.* **101**, 216103 (2008).
19. Stöger, B. *et al.* Point defects at cleaved $\text{Sr}_{n+1}\text{Ru}_n\text{O}_{3n+1}(001)$ surfaces. *Phys. Rev. B* **90**, 165438 (2014).
20. Iwaya, K. *et al.* Local Tunneling Spectroscopy across a Metamagnetic Critical Point in the Bilayer Ruthenate $\text{Sr}_3\text{Ru}_2\text{O}_7$. *Phys. Rev. Lett.* **99**, 057208 (2007).
21. Barker, B. I. *et al.* STM studies of individual Ti impurity atoms in Sr_2RuO_4 . *Phys. B Condens. Matter* **329–333**, 1334–1335 (2003).
22. Kambara, H. *et al.* Scanning Tunneling Microscopy and Spectroscopy of Sr_2RuO_4 . in *AIP Conference Proceedings* vol. 850 539–540 (AIP, 2006).
23. Wang, Z. *et al.* Quasiparticle interference and strong electron–mode coupling in the quasi-one-dimensional bands of Sr_2RuO_4 . *Nat. Phys.* **13**, 799–805 (2017).
24. Sacks, W., Roditchev, D. & Klein, J. Voltage-dependent STM image of a charge density wave. *Phys. Rev. B* **57**, 13118 (1998).
25. Puetter, C. M., Rau, J. G. & Kee, H.-Y. Microscopic route to nematicity in $\text{Sr}_3\text{Ru}_2\text{O}_7$. *Phys. Rev. B* **81**, 081105 (2010).
26. Scaffidi, T., Romers, J. C. & Simon, S. H. Pairing symmetry and dominant band in Sr_2RuO_4 . *Phys. Rev. B* **89**, 220510 (2014).
27. Van Hove, L. The Occurrence of Singularities in the Elastic Frequency Distribution of a Crystal. *Phys. Rev.* **89**, 1189–1193 (1953).

28. Bergemann, C., Mackenzie, A. P., Julian, S. R., Forsythe, D. & Ohmichi, E. Quasi-two-dimensional Fermi liquid properties of the unconventional superconductor Sr_2RuO_4 . *Adv. Phys.* **52**, 639–725 (2003).
29. Matzdorf, R., Ismail, Kimura, T., Tokura, Y. & Plummer, E. W. Surface structural analysis of the layered perovskite Sr_2RuO_4 by LEED $I(V)$. *Phys. Rev. B* **65**, 085404 (2002).
30. Tamai, A. *et al.* Fermi Surface and van Hove Singularities in the Itinerant Metamagnet $\text{Sr}_3\text{Ru}_2\text{O}_7$. *Phys. Rev. Lett.* **101**, 026407 (2008).
31. Ikeda, S.-I., Maeno, Y., Nakatsuji, S., Kosaka, M. & Uwatoko, Y. Ground state in $\text{Sr}_3\text{Ru}_2\text{O}_7$: Fermi liquid close to a ferromagnetic instability. *Phys. Rev. B* **62**, R6089–R6092 (2000).
32. Chubukov, A. Pairing Mechanism in Fe-Based Superconductors. *Annu. Rev. Condens. Matter Phys.* **3**, 57–92 (2012).
33. Keimer, B., Kivelson, S. A., Norman, M. R., Uchida, S. & Zaanen, J. From quantum matter to high-temperature superconductivity in copper oxides. *Nature* **518**, 179–186 (2015).
34. Hicks, C. W. *et al.* Strong Increase of T_c of Sr_2RuO_4 Under Both Tensile and Compressive Strain. *Science* **344**, 283–285 (2014).

Acknowledgments:

We would like to thank J. Betouras, S. Grigera, C. Hooley, P. King and S. Simon for fruitful discussions and David Miller for TEM characterization of the samples.

CAM acknowledges funding from EPSRC through EP/L015110/1, LCR from the Royal Commission for the Exhibition of 1851, AWR from EPSRC through EP/P024564/1, PW from EPSRC through EP/R031924/1, and CMY and PW through EP/S005005/1. VG, RF, RB, AG, AV and PW acknowledge support from a Bilateral Project 2019-2020 in a joint RSE/CNR scheme (CUP B56C18003920005).

Author contributions:

Competing interests: The authors declare no competing interests.

Data availability: Underpinning data will be made available at <http://doi.org/xxx>.

Supplementary Material for

The surface layer of Sr_2RuO_4 : A two-dimensional model system for magnetic-field-tuned quantum criticality

Carolina A. Marques,^{1,*} Luke C. Rhodes,^{1,*} Rosalba Fittipaldi,²
Veronica Granata,³ Chi Ming Yim,¹ Renato Buzio,⁴ Andrea Gerbi,⁵
Antonio Vecchione,² Andreas W. Rost,^{1,6} and Peter Wahl^{1,†}

*¹School of Physics and Astronomy,
University of St Andrews, North Haugh,
St Andrews, KY16 9SS, United Kingdom*

²CNR-SPIN, UOS Salerno, Via Giovanni Paolo II 132, Fisciano, I-84084, Italy.

*³Dipartimento di Fisica “E. R. Caianiello,
” Università di Salerno, I-84084 Fisciano, Salerno, Italy.*

*⁴CNR-SPIN Institute for Superconductors, Innovative Materials,
and Devices, Corso F.M. Perrone 24, Genova, 16152, Italy*

⁵CNR-SPIN, Corso F.M. Perrone 24, Genova, 16152, Italy

*⁶Max-Planck-Institute for Solid State Research,
Heisenbergstr. 1, 70569 Stuttgart, Germany*

This PDF file includes:

Materials and Methods (S1)

Differential conductance maps (S2)

Tight-binding model (S3)

Analysis of magnetic-field dependent tunneling spectra (S4)

Figs. S1 to S7

*These authors contributed equally.

†correspondence to: wahl@st-andrews.ac.uk

S1. MATERIALS AND METHODS

A. Single crystal growth.

The Sr_2RuO_4 crystals used in this work were grown by the floating-zone technique with Ru self-flux, using a commercial image furnace with double-elliptical mirrors and two 2.0kW halogen lamps (S1). Morphological and elemental characterization of the crystals was carried out using a Zeiss Leo EVO 50 scanning electron microscope (SEM) equipped with an Oxford INCA Energy 300 energy dispersive X-ray spectroscopy (EDS) system. The structure and crystalline qualities of the samples were assessed by a high-resolution X-ray diffractometer (Panalytical, X Pert MRD), with a Cu K- α source.

B. Characterization

1. Transmission electron microscopy (TEM)

To verify the crystal quality in the surface region following cleavage of the sample in the STM, we have performed Transmission Electron Microscopy on a sample on which STM measurements had been carried out. The sample for STEM analysis was prepared by conventional gallium focused ion beam (FIB) milling using an FEI Scios focused ion beam scanning electron microscope (FIBSEM) equipped with an EDAX Hikari Super electron back-scattered diffraction (EBSD) detector. The orientation of the sample was determined by EBSD prior to milling, to cut a lamella in the [010] plane. High angle annular dark field (HAADF) images were recorded using a probe corrected FEI Themis 200 scanning/transmission electron microscope operated at 200kV.

Figure S1(a) shows a TEM image of a cross section of the sample after cleaving. It shows a uniform phase along the c -axis on the scale of $\approx 80\text{nm}$ extending up to the surface. Figure S1B shows a zoom in with atomic resolution. It shows the expected stacking for Sr_2RuO_4 , as evidenced by the inset, where both Strontium and Ruthenium atoms are visible, with the Ru atoms appearing with a slightly higher intensity. Oxygen atoms are not visible. The TEM image shows no evidence of inclusions of other members of the Ruddlesden-Popper series (i.e. $\text{Sr}_{n+1}\text{Ru}_n\text{O}_{3n+1}$ with $n > 1$).

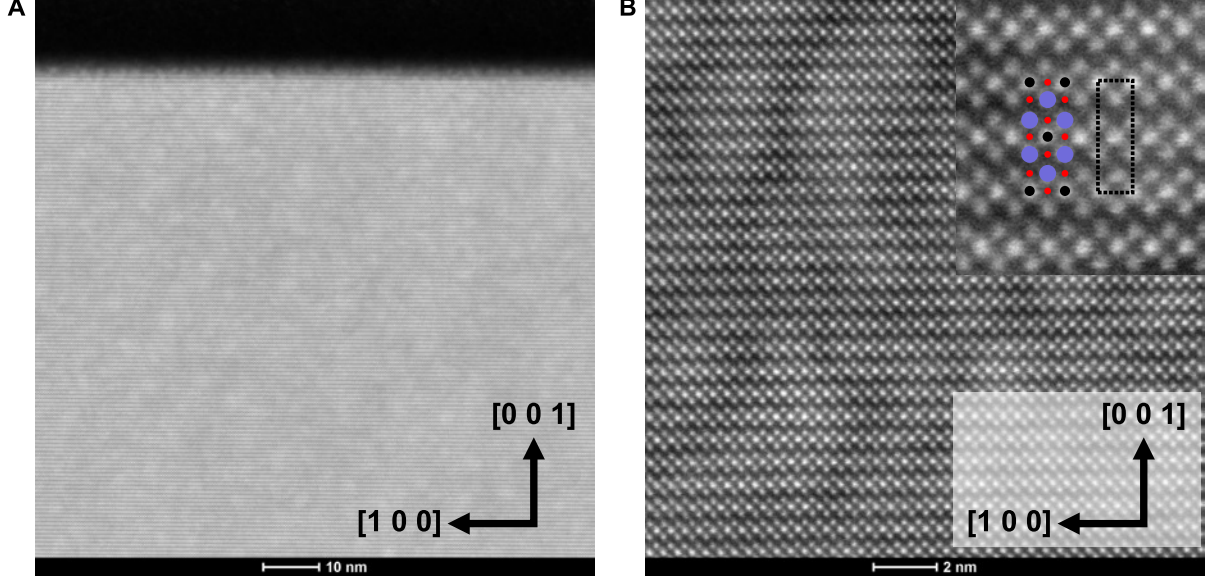


FIG. S1: TEM images along the b-axis. (A) Image of the cross-section of a sample after STM measurements have been performed on its surface, demonstrating uniformity up to the surface. (B) High-resolution image showing atomic resolution. The inset shows a zoom in of the image, with the stacking expected for Sr_2RuO_4 . Superimposed to the TEM image is the atomic structure, with purple spheres indicating strontium atoms, black ones ruthenium atoms and red ones oxygen atoms. The black dashed line delimits the unit cell of Sr_2RuO_4 .

2. Resistance measurements

Electric transport measurements were performed using a four probe technique with a ^3He refrigerator. The resistance as a function of temperature shows a superconducting transition at $T_C = 1.5$ K, in agreement with data reported in literature for good quality crystals(S2).

We determine a residual-resistance ratio (RRR) $\lim_{T \rightarrow 0\text{K}} \frac{R(300\text{K})}{R(T)} \approx 666$, extrapolated to 0K from fitting the resistance above T_C to $R(T) = R_{\text{res}} + AT^2$ (Figure S2A). This value is comparable to that of high-purity crystals reported in the literature(S3).

3. Scanning tunneling microscopy (STM)

Experiments were performed in a home-built ultra-low temperature STM operating in a dilution refrigerator.(S4) Samples were prepared by *in-situ* cleaving at low temperatures ($\sim 20\text{K}$) in cryogenic vacuum. We used STM tips cut from PtIr wire, and prepared them *in-*

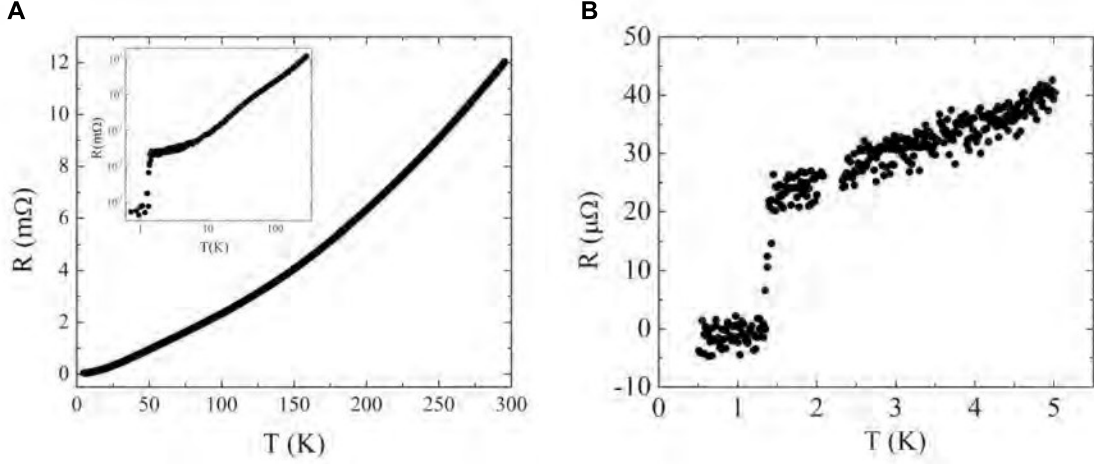


FIG. S2: **Resistance as a function of temperature of Sr₂RuO₄ crystal measured applying a bias current along the a-b plane.** (A) Resistance up until room temperature. The inset shows the resistance as function of temperature in log-log scale (B) Low temperature resistance down to 0.5 K showing a superconducting transition at 1.5 K.

situ by field emission on a Au(111) single crystal. Bias voltages were applied to the sample, with the tip at virtual ground.

Spectroscopic measurements were performed using a lock-in amplifier to measure differential conductance $g(V)$. The bias voltage V was modulated at a frequency of $\nu = 397\text{Hz}$, the RMS amplitude V_L is given in figure captions where applicable. The bias and current setpoints, V_{set} and I_{set} respectively, are indicated for both topographies and spectroscopic maps.

After cleaving and inserting the samples into the STM head, we have always observed the reconstructed SrO termination as observed in previous reports(*S5–S8*) and as can be inferred from the appearance of the defects.

S2. DIFFERENTIAL CONDUCTANCE MAPS

In this section, we show the real space conductance maps underpinning the data shown in fig. 2D and how it has been processed.

A. Real space maps

The topographic image acquired simultaneously with the map taken at 2K is shown in Figure S3A and the corresponding real space differential conductance map, $g(\mathbf{r}, V) = dI/dV(\mathbf{r}, V)$, for $V = -3.4\text{mV}$ in Figure S3B. The checkerboard charge order is clearly visible. In addition quasiparticle interference (QPI) effects are observed around the defect seen in the topography.

B. Processing of differential conductance maps

In Figure S3 we show images following each step of the data processing. The raw Fourier transformation of the $g(\mathbf{r}, V)$ map is displayed in Fig. S3C. It shows clear signatures of the atomic peaks at $(\pm 2\pi, 0)$ and $(0, \pm 2\pi)$ (in units of $1/a$, where a is the lattice constant of the bulk tetragonal unit cell), as well as of the checkerboard charge order at $(\pm\pi, \pm\pi)$ and $(\pm\pi, \pm\pi)$. There are in addition weak higher order peaks. The Fourier transformation is first corrected for any linear drift by mapping the atomic peaks onto a perfect square (Fig. S3D). Next, the resulting images are mirror symmetrized along the horizontal or vertical direction (Fig. S3E). Finally, to suppress the high intensity at the centre of the image due to the distribution of defects, a Gaussian function with a width of 4 pixels is subtracted (Fig. S3F).

This procedure was implemented for all layers of the map. Fig. S4 shows the Fourier transformation after processing of the same $g(\mathbf{r}, V)$ map at different energies, between -8.2mV and $+7.8\text{mV}$. The intensity of the $(\pm\pi, \pm\pi)$ peaks is strongly energy dependent, showing maximum intensity at -3.4mV (highlighted by a red box). Additionally, we observed an anisotropy in the intensities of the $(2\pi, 0)$ and $(0, 2\pi)$ peaks, as is indicated in Fig. S4 by the solid red and dashed white circles. It can be seen that the high intensity switches from one direction to the other with energy. This reflects the atomic scale symmetry breaking shown in Fig. 3B and C in the main text.

C. Phase-referenced Fourier transformation

In fig. 2D of the main text, we show a phase-referenced Fourier transformation to deduce the characteristic energy scale of the checkerboard charge order and the relative phase at positive and negative bias voltages. The Fourier transformation $\tilde{g}(\mathbf{q}, V)$ of a differential

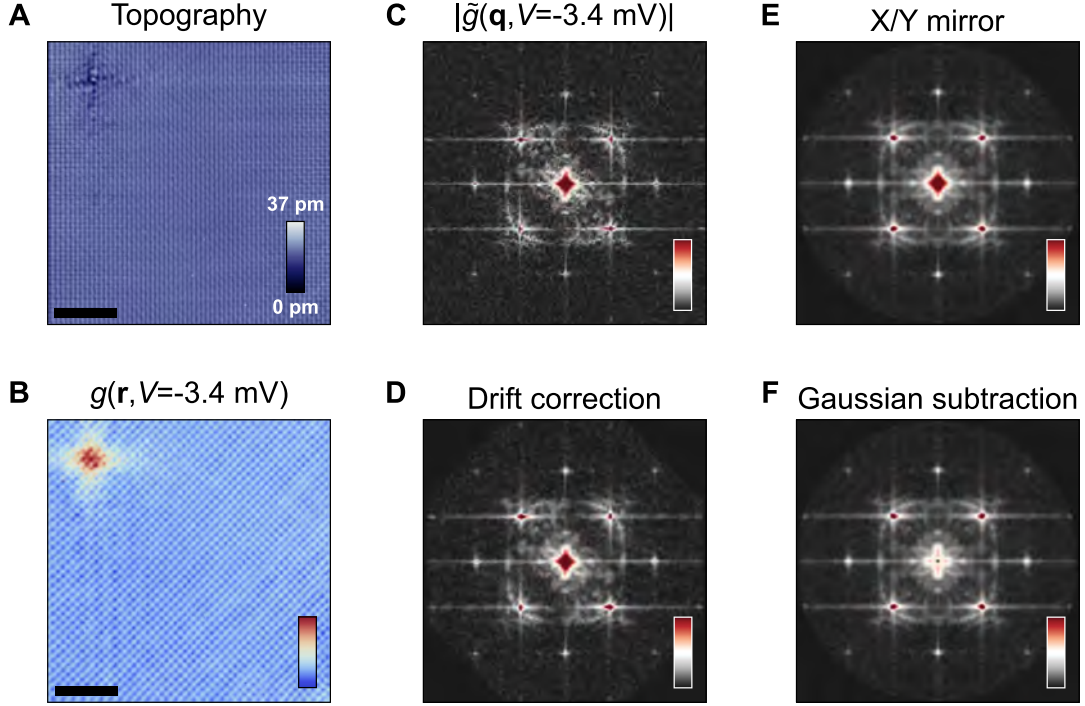


FIG. S3: **Processing of differential conductance maps.** (A) Topography acquired simultaneously with map, showing one defect in the top left corner. Scale bar: 5nm ($V_{\text{set}} = 7.8\text{mV}$, $I_{\text{set}} = 225\text{pA}$). (B) Real space $g(\mathbf{r}, V)$ at $V = -3.4\text{ mV}$. (C) Absolute value of its Fourier transformation, $|\tilde{g}(\mathbf{q}, V)|$, (D) after drift correction, (E) after symmetrizing along the horizontal (or vertical) direction, and (F) after subtraction of a gaussian function with a width of 4 pixels at the centre of the image ($V_L = 800\mu\text{V}$, $T = 2\text{K}$, $B_z = 0\text{T}$).

conductance map $\tilde{g}(\mathbf{r}, V)$ which shows the atomic lattice exhibits two pairs of Bragg peaks at $\mathbf{q}_{\text{at}} = (\pm 2\pi, 0)$ and $(0, \pm 2\pi)$ (in units of $1/a$, where a is the lattice constant), as shown in Figure S5A by the black circle. The checkerboard order shown in Figure 2B, C of the main text has a wavelength that is $\sqrt{2}$ times larger, with the unit vector 45° rotated. The periodicity due to the checkerboard charge order shows up as four peaks at $\mathbf{q}_{CKB} = (\pm\pi, \pm\pi)$, one of which is indicated by the red circle in Fig. S5A. The amplitude of this checkerboard order is reflected in the intensity of Fourier peak, $|\tilde{g}(\mathbf{q}_{CKB}, V)|$, as shown in Fig. S4. We can determine the characteristic energy scale of the checkerboard modulation as a function of energy by plotting, $|\tilde{g}(\mathbf{q}_{CKB}, V)|$ as a function of applied bias V , however losing the phase information ϕ contained in the Fourier transformation contained in the

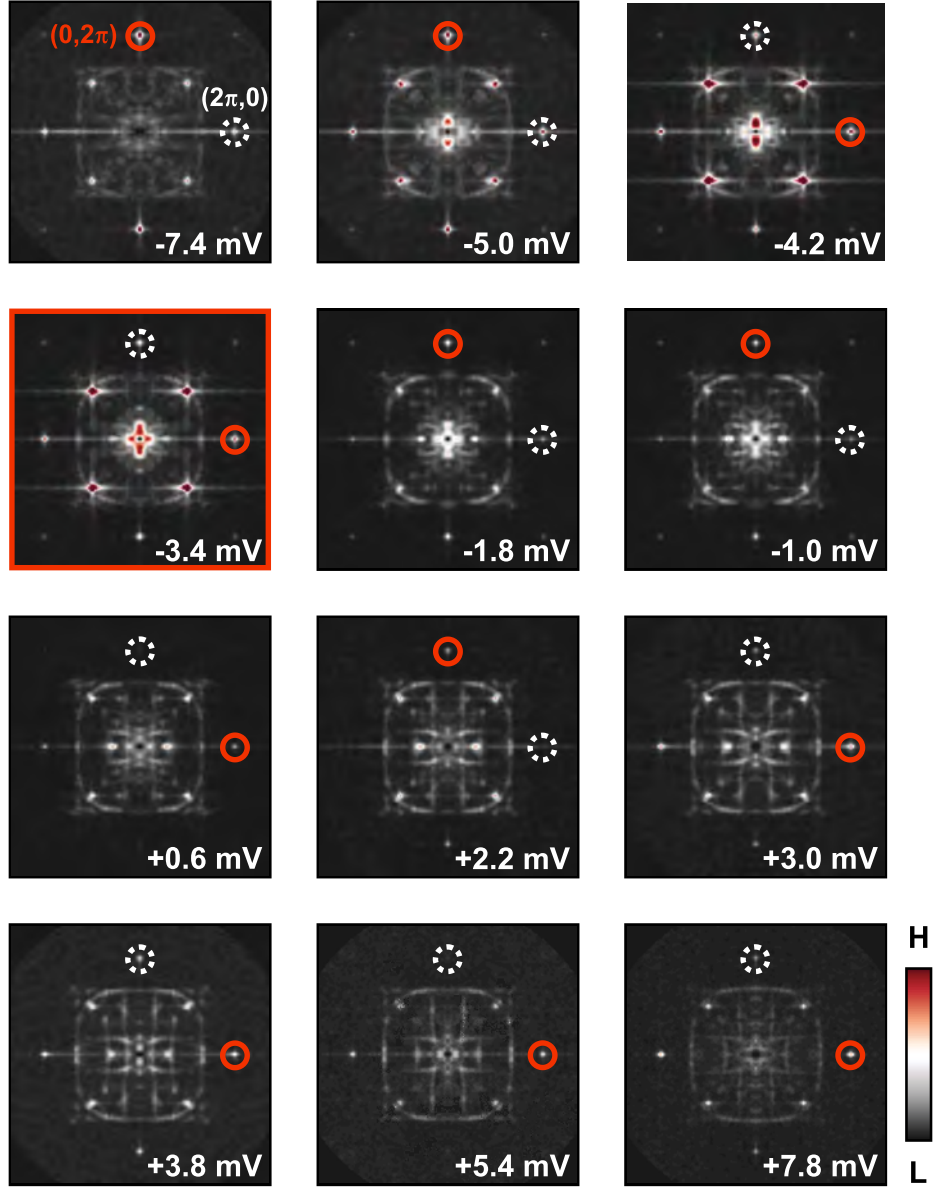


FIG. S4: **Energy layers from the $\tilde{g}(\mathbf{q}, V)$ map** shown in Fig. 2 of the main text and Fig. S3. The intensity of the peaks at $\mathbf{q}_{\text{CKB}} = (\pm\pi, \pm\pi)$ due to the checkerboard charge order is strongly energy dependent. The layer corresponding to the energy of the vHs is highlighted by a red box, where the peaks at \mathbf{q}_{CKB} exhibit the highest intensity. Additionally, the intensity of the Bragg peaks $\mathbf{q}_{\text{at}} = (0, \pm 2\pi)$ and $(\pm 2\pi, 0)$ switches with energy due to the nematicity (cf. fig. 3B, C of the main text). For each layer, the higher intensity peak is highlighted by a red circle, and the lower intensity peak with a dashed white circle. The color bar for all images is scaled to the same range.

complex values of

$$\tilde{g}(\mathbf{q}, V) = |\tilde{g}(\mathbf{q}, V)| e^{i\phi(\mathbf{q}, V)}. \quad (\text{S1})$$

While analyzing the phase ϕ is possible, it suffers from an overall global phase factor which is arbitrary. To remove this global phase factor, we use a phase-referenced Fourier transformation (PR-FFT)(S9)

$$\tilde{g}^R(\mathbf{q}, V) = \frac{\tilde{g}(\mathbf{q}, V)}{e^{i\phi(\mathbf{q}, V_0)}} = |\tilde{g}(\mathbf{q}, V)| e^{i(\phi(\mathbf{q}, V) - \phi(\mathbf{q}, V_0))}. \quad (\text{S2})$$

In this PR-FT, the phase at each \mathbf{q} -vector is referenced to the phase at a specific energy V_0 , removing the global phase factor. This allows tracking of the change in phase as a function of energy relative to that layer by simply plotting the real part of the PR-FT

$$\text{Re} [\tilde{g}^R(\mathbf{q}, V)] = |\tilde{g}(\mathbf{q}, V)| \cos (\phi(\mathbf{q}, V) - \phi(\mathbf{q}, V_0)). \quad (\text{S3})$$

Here, we reference the phase to the map layer at $V_0 = -3.4\text{mV}$. The real part of the PR-FFT images, Figure S5C, $\text{Re}[\tilde{g}^R((\pi, \pi), V)]$ allows us to determine if there is a phase shift between the checkerboard order at different energies as well as the relative amplitude. A phase reversal means a change in sign. At the reference energy, V_0 , $\text{Re}[\tilde{g}^R((\pi, \pi), V_0)]$ will be positive by definition. Fig. S5C shows $\text{Re}[\tilde{g}^R((\pi, \pi), V = +3\text{mV})]$, where the peaks at \mathbf{q}_{CKB} appear with a negative sign, evidencing a phase shift with respect to the charge modulation at $V_0 = -3.4\text{mV}$. Figure 2D of the main text shows that the checkerboard order appears predominantly at $V = -3.5\text{mV}$ and $V = 3.5\text{mV}$ with opposite phase. For better comparison between the maps at the two different temperatures, $\tilde{g}^R(\mathbf{q}_{\text{CKB}}, V)$ was normalized by its value, $\tilde{g}^R(\mathbf{q}_{\text{CKB}}, V_s)$, at the bias setpoint, V_s . This was $V_{\text{set}} = 7.8\text{ mV}$ for the map measured at 2 K and $V_{\text{set}} = 7.0\text{ mV}$ for the one at 59 mK.

S3. TIGHT-BINDING MODEL

The tight binding model for the surface of Sr_2RuO_4 may be defined, in an analogous manner to that of the bulk, via hopping associated with the three t_{2g} Ru orbitals (S10),

$$H^\sigma(\mathbf{k}) = \begin{pmatrix} E_{xz}(\mathbf{k}) & \gamma(\mathbf{k}) - \sigma i\eta & i\eta \\ \gamma(\mathbf{k}) + \sigma i\eta & E_{yz}(\mathbf{k}) & -\sigma\eta \\ -i\eta & -\sigma\eta & E_{xy}(\mathbf{k}) \end{pmatrix}. \quad (\text{S4})$$

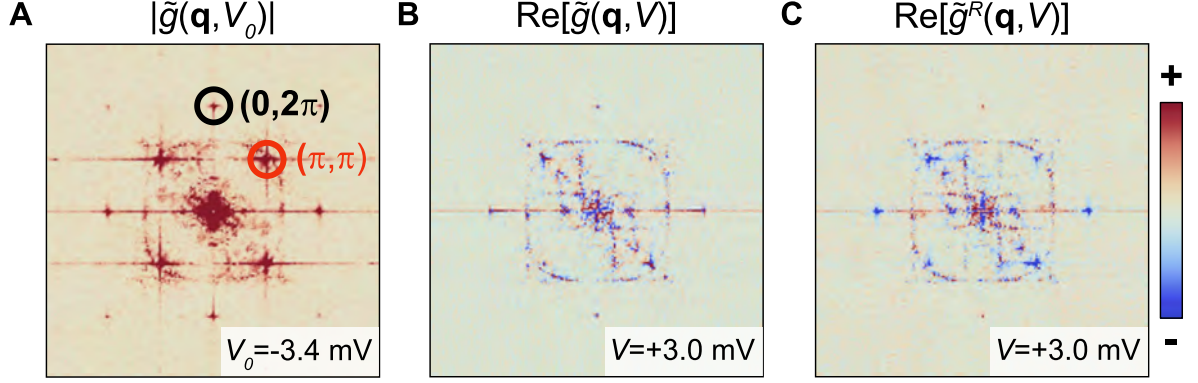


FIG. S5: **Phase-referenced Fourier transformation.** (A) Amplitude $|\tilde{g}(\mathbf{q}, V_0 = -3.4\text{mV})|$ for the Fourier transformation. (B) Real part $\text{Re}[\tilde{g}(\mathbf{q}, V = +3.0\text{mV})]$, it can be seen that the peaks at (π, π) and $(-\pi, \pi)$ have opposite sign. (C) Real part of the PR-FFT, $\text{Re}[\tilde{g}^R(\mathbf{q}, V = +3.0\text{mV})]$, showing the reversed sign of the peaks at (π, π) and $(-\pi, \pi)$ compared to panel A (map parameters as in fig. S3).

This Hamiltonian includes nearest neighbour hoppings between the d_{xz} and d_{yz} orbitals as well as up to third nearest neighbour hoppings between d_{xy} orbitals,

$$\begin{aligned}
E_{xz}(\mathbf{k}) &= -2t_1 \cos(k_x) - 2t_2 \cos(k_y) - \mu, \\
E_{yz}(\mathbf{k}) &= -2t_2 \cos(k_x) - 2t_1 \cos(k_y) - \mu, \\
E_{xy}(\mathbf{k}) &= -2t_3(\cos(k_x) + \cos(k_y)) - 4t_4 \cos(k_x) \cos(k_y) - 2t_5(\cos(2k_x) + \cos(2k_y)) - \mu_c.
\end{aligned}
\tag{S5}$$

The off diagonal term, $\gamma(\mathbf{k})$, describes inter-orbital hopping between the degenerate d_{xz} and d_{yz} states and is written as $\gamma(\mathbf{k}) = -4t_{inter} \sin(k_x) \sin(k_y)$. The rest of the off-diagonal terms arise from the spin-orbit interaction, where η is the spin-orbit coupling constant and σ is defined as $+1$ for up spins (\uparrow) and -1 for down spins (\downarrow).

Using this basis, a tight binding model for the Ru electronic structure can be defined via the Hamiltonian

$$H_{\text{Ru}}(\mathbf{k}) = \begin{pmatrix} H^\uparrow(\mathbf{k}) & 0 \\ 0 & H^\downarrow(\mathbf{k}) \end{pmatrix}, \quad (\text{S6})$$

representing now a 6×6 matrix. For the surface, we must account for the doubling of the unit cell due to the additional octahedra rotation. This surface tight binding model is then given by the 12×12 matrix

$$H_{\text{surf}}(\mathbf{k}) = \begin{pmatrix} H_{\text{Ru}}(\mathbf{k}) & 0 \\ 0 & H_{\text{Ru}}(\mathbf{k} + \mathbf{Q}) \end{pmatrix}, \quad (\text{S7})$$

with $\mathbf{Q} = (\pi, \pi)$.

For the bulk tight binding model, presented in Fig. 1B of the main text, we calculate the Eigenvalues using Eq. S6 with the hopping parameters from Ref. *S10*.

$$\begin{aligned} t_1 &= 0.15\text{eV} & t_2 &= 0.1t_1 & t_3 &= 0.8t_1 & t_4 &= 0.3t_1 & t_5 &= 0.1t_1 \\ t_{\text{inter}} &= 0.01t_1 & \mu &= 1.0t_1 & \mu_c &= 1.1t_1 & \eta &= 0.1t_1. \end{aligned}$$

Here t_1 is set to 150meV and all other parameters are defined relative to t_1 .

For the surface tight binding description, which has been used in Fig. 4 of the main text, we use $t_5 = 0.095t_1$, $\mu = 0.75t_1$ and $\mu_c = 0.812t_1$. This places the vHs just above the Fermi level and slightly alters the Fermi wave vector k_F of the d_{xz} and d_{yz} bands to best fit the ARPES data (*S11*). We introduce a hybridisation between the two Ru site, $\Delta_{\text{hyb}} = 3\text{meV}$, as off-diagonal elements in Eq. S7,

$$H_{\text{surf}}(\mathbf{k}) = \begin{pmatrix} H_{\text{Ru}}(\mathbf{k}) & \Delta_{\text{hyb}}\hat{I} \\ \Delta_{\text{hyb}}^*\hat{I} & H_{\text{Ru}}(\mathbf{k} + \mathbf{Q}) \end{pmatrix}, \quad (\text{S8})$$

and include a phenomenological C_4 symmetry breaking term $\Delta_{\text{nem}}(\mathbf{k}) = \delta_{\text{nem}}(\cos(k_x) - \cos(k_y))$ specifically to the d_{xy} orbital in H_{Ru} , with $\delta_{\text{nem}} = 2 \text{ meV}$, to produce the full Hamiltonian defined in Eq. 1 of the main text. A similar nematic term has been discussed for $\text{Sr}_3\text{Ru}_2\text{O}_7$ previously. (*S12*)

$$H_{\text{surf}}(\mathbf{k}) = \begin{pmatrix} H_{\text{Ru}}(\mathbf{k}) + \Delta_{\text{nem}}(\mathbf{k})\hat{I}_{xy} & \Delta_{\text{hyb}}\hat{I} \\ \Delta_{\text{hyb}}^*\hat{I} & H_{\text{Ru}}(\mathbf{k} + \mathbf{Q}) + \Delta_{\text{nem}}(\mathbf{k} + \mathbf{Q})\hat{I}_{xy} \end{pmatrix}. \quad (\text{S9})$$

The density of states presented in Fig. 4B has been calculated via

$$N_0(\omega) = -\frac{1}{\pi} \text{Tr} \left[\text{Im} \left[\sum_{\mathbf{k}} G(\mathbf{k}, \omega) \right] \right]. \quad (\text{S10})$$

Here, $G(\mathbf{k}, \omega)$ is the Green's function defined as $G(\mathbf{k}, \omega) = \frac{1}{\omega - H(\mathbf{k}) + i\Gamma}$, where ω is the energy and Γ a broadening parameter. We use a \mathbf{k} -grid of 4096x4096 lattice points and $\Gamma = 0.1$ meV.

Fig. S6 shows the Fermi surface, band structure and DOS given by the tight-binding model described above for comparison. Fig. S6A-C show the case where only the doubling of the unit cell is taken into account (Eq. S7). The vHs was put above, but very close to, E_F and it appears as a sharp peak with logarithmic divergence, cut off by the broadening Γ . Fig. S6D-F show the case where only the C_4 -symmetry breaking term is included. The d_{xy} band becomes C_2 -symmetric, and the vHs splits into two peaks, one above E_F and another below, although no gap opens around the Fermi energy. Fig. S6G-I show the case of eq. S9, where both the nematic term and the hybridization potential are included. A gap is opened between the d_{xy} bands, creating four vHs. The calculated DOS reproduces the measured differential conductance spectrum, as shown in Fig. 4 of the main text.

S4. ANALYSIS OF MAGNETIC-FIELD DEPENDENT TUNNELING SPECTRA

Each $g(\mathbf{r}, V)$ spectrum shown in Figure 4C of the main text is obtained from an average of 10 spectra. All spectra were acquired with the same setpoint conditions before turning off the feedback loop. To determine the energy of the van Hove singularity from the peak positions in the spectra, we first subtract a background from the spectra, and then fit the positions of the dominant peaks. To describe the background, we fit an arc tangent and a constant ($f(V) = a \cdot \arctan[(V - V_0)/\Gamma] + c$) to the background in the data at 13.4T to describe the gap edge at negative energies and subtract the resulting function $f(V)$ as a base line. For the data at other fields, we fit the values of a and c to the background using the same arctangent function, but keep V_0 and Γ fixed at the values of the fit at 13.4T, Figure S7A. To determine the energy of the magnetic field split van Hove singularity, we fit a Lorentzian, Figure S7B.

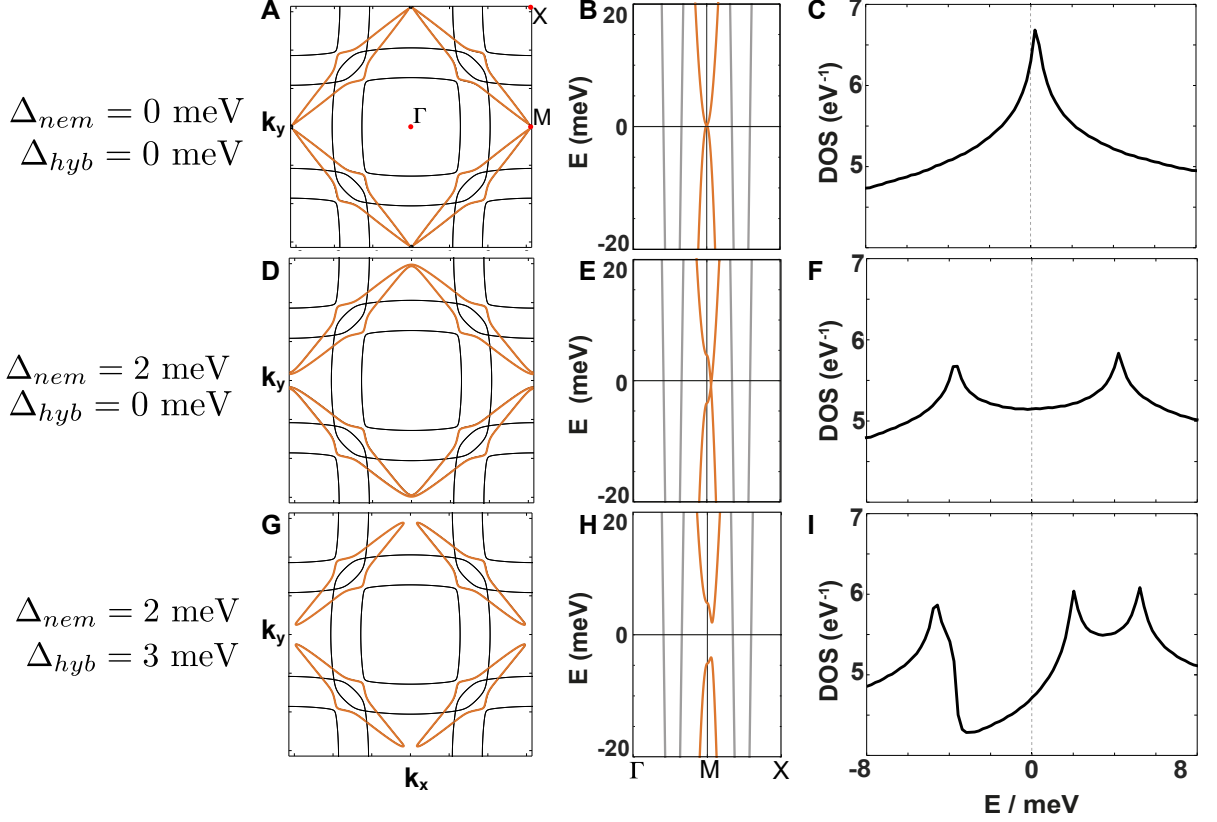


FIG. S6: Tight-binding model of the surface of Sr_2RuO_4 . (A-C) Fermi surface, band dispersion along Γ -M-X and density of states between $\pm 8 \text{ meV}$ for a model without nematicity ($\Delta_{nem} = 0 \text{ meV}$) and hybridization of bands due to the reconstruction $\Delta_{hyb} = 0 \text{ meV}$. (D-F) Equivalent plots with nematicity included, $\Delta_{nem} = 2 \text{ meV}$, but no hybridization between the bands due to the reconstruction $\Delta_{hyb} = 0 \text{ meV}$. (G-I) Equivalent plots with nematicity $\Delta_{nem} = 2 \text{ meV}$ (as before) and a non-zero hybridization $\Delta_{hyb} = 3 \text{ meV}$.

-
- S1. R. Fittipaldi, A. Vecchione, S. Fusanobori, K. Takizawa, H. Yaguchi, J. Hooper, R. Perry, and Y. Maeno, *Journal of Crystal Growth* **282**, 152 (2005), ISSN 0022-0248, URL <http://www.sciencedirect.com/science/article/pii/S0022024805005841>.
- S2. M. E. Barber, A. S. Gibbs, Y. Maeno, A. P. Mackenzie, and C. W. Hicks, *Phys. Rev. Lett.* **120**, 076602 (2018), URL <https://link.aps.org/doi/10.1103/PhysRevLett.120.076602>.
- S3. A. P. Mackenzie, R. K. W. Haselwimmer, A. W. Tyler, G. G. Lonzarich, Y. Mori, S. Nishizaki,

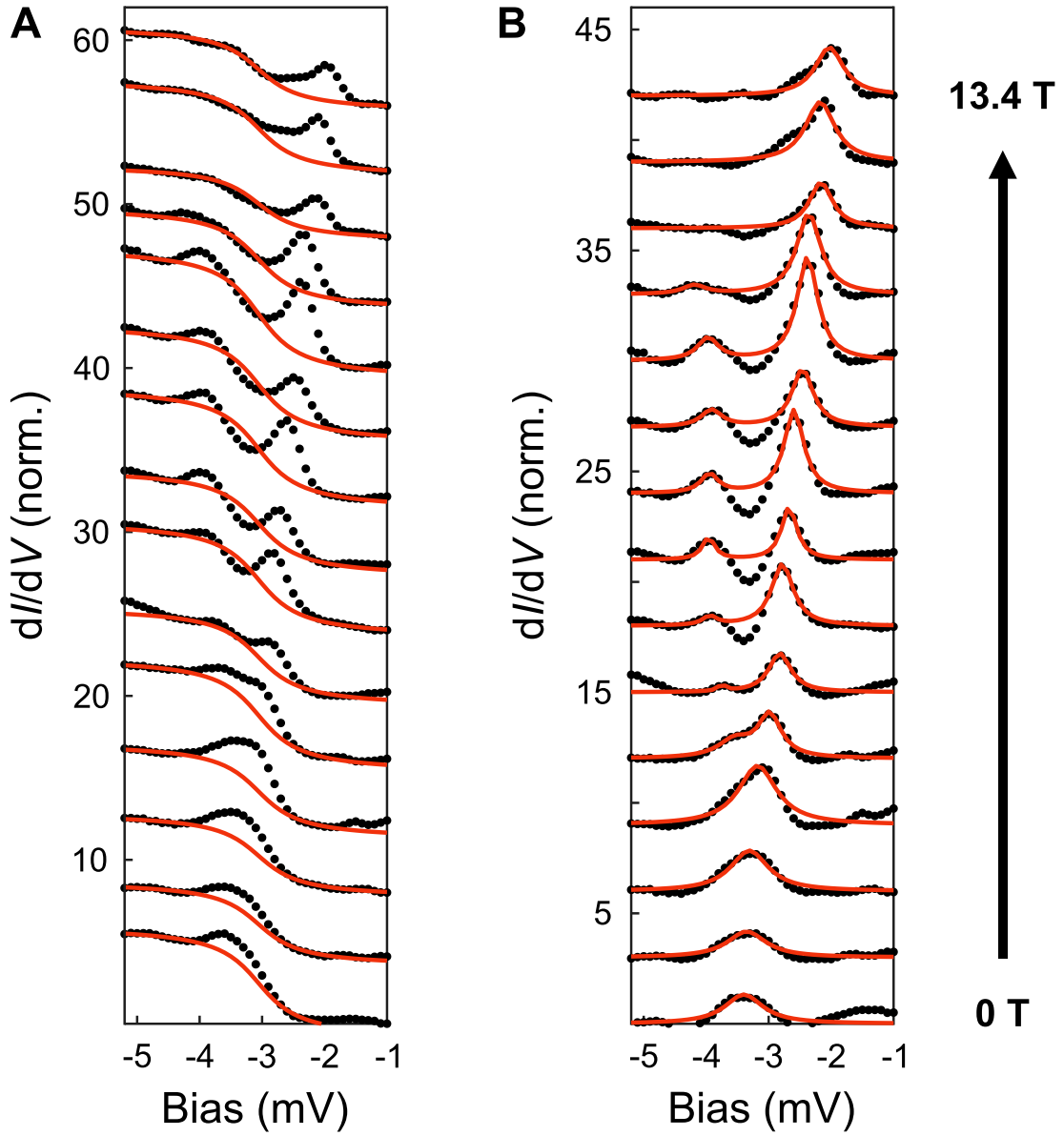


FIG. S7: **Determination of splitting of vHs in magnetic field.** (A) $g(\mathbf{r}, V)$ spectra in magnetic fields of $B = 0 \dots 13.4\text{T}$, with the background fit shown as red lines. (B) $g(\mathbf{r}, V)$ spectra after subtraction of the background. The red lines show the lorentzian fits to extract the peaks positions.

and Y. Maeno, Phys. Rev. Lett. **80**, 161 (1998), URL <https://link.aps.org/doi/10.1103/PhysRevLett.80.161>.

S4. U. R. Singh, M. Enayat, S. C. White, and P. Wahl, Review of Scientific Instruments **84**, 013708 (2013).

- S5. B. Barker, S. Dutta, C. Lupien, P. McEuen, N. Kikugawa, Y. Maeno, and J. Davis, *Physica B: Condensed Matter* **329-333**, 1334 (2003), ISSN 09214526, URL <http://linkinghub.elsevier.com/retrieve/pii/S0921452602021580>.
- S6. Y. Pennec, N. J. C. Ingle, I. S. Elfimov, E. Varene, Y. Maeno, A. Damascelli, and J. V. Barth, *Phys. Rev. Lett.* **101**, 216103 (2008), ISSN 0031-9007, 1079-7114, URL <https://link.aps.org/doi/10.1103/PhysRevLett.101.216103>.
- S7. B. Stöger, M. Hieckel, F. Mittendorfer, Z. Wang, M. Schmid, G. S. Parkinson, D. Fobes, J. Peng, J. E. Ortmann, A. Limbeck, et al., *Phys. Rev. B* **90**, 165438 (2014), ISSN 1098-0121, 1550-235X, URL <https://link.aps.org/doi/10.1103/PhysRevB.90.165438>.
- S8. Z. Wang, D. Walkup, P. Derry, T. Scaffidi, M. Rak, S. Vig, A. Kogar, I. Zeljkovic, A. Husain, L. H. Santos, et al., *Nature Physics* **13**, 799 (2017), ISSN 1745-2473, 1745-2481, URL <http://www.nature.com/articles/nphys4107>.
- S9. S. Chi, W. N. Hardy, R. Liang, P. Dosanjh, P. Wahl, S. A. Burke, and D. A. Bonn, arXiv:1710.09088 [cond-mat] (2017), arXiv: 1710.09088, URL <http://arxiv.org/abs/1710.09088>.
- S10. T. Scaffidi, J. C. Romers, and S. H. Simon, *Phys. Rev. B* **89**, 220510 (2014), URL <https://link.aps.org/doi/10.1103/PhysRevB.89.220510>.
- S11. A. Tamai, M. Zingl, E. Rozbicki, E. Cappelli, S. Riccò, A. de la Torre, S. McKeown Walker, F. Y. Bruno, P. D. C. King, W. Meevasana, et al., *Phys. Rev. X* **9**, 021048 (2019), URL <https://link.aps.org/doi/10.1103/PhysRevX.9.021048>.
- S12. C. Puetter, H. Doh, and H.-Y. Kee, *Phys. Rev. B* **76**, 235112 (2007), ISSN 1098-0121, 1550-235X, URL <https://link.aps.org/doi/10.1103/PhysRevB.76.235112>.